

Topographic evolution of heat-treated Nb upon electropolishing for superconducting rf applications

Eric M. Lechner^{1,*}, Jonathan W. Angle², Carrie Baxley,¹
Michael J. Kelley^{1,2} and Charles E. Reece¹

¹Thomas Jefferson National Accelerator Facility, Newport News, Virginia 23606, USA

²Nanoscale Characterization and Fabrication Laboratory, Virginia Polytechnic Institute and State University, 1991 Kraft Drive, Blacksburg, Virginia 24061, USA

 (Received 27 July 2023; accepted 15 September 2023; published 10 October 2023)

Surface finish plays an essential role in the performance of superconducting radio frequency cavities. Several surface treatments have been developed to reduce surface resistance at a moderate accelerating gradient. We investigated the effects of sequential electropolishing on samples vacuum heat-treated at 300 and 600 °C and N-doped Nb samples using atomic force microscopy. The N-doping process precipitates niobium nitrides within grains and, most notably, continuously and deeply along some grain boundaries. Upon electropolishing, the nitrides are preferentially removed leaving behind a topographically imperfect surface marked by relatively deep holes and grooves with low radius of curvature edges. The progression of magnetic field enhancement and superheating field suppression factors upon electropolishing were investigated using atomic force micrographs. While minor changes in magnetic field enhancement and superheating field suppression factors are observed for the 300 and 600 °C heat-treated Nb, substantial improvements are observed for N-doped Nb. In this system, the most severe topographic defects are the grain boundary grooves which substantially suppress the superheating field. We find that the severity of topographic defects is related to the N-doping process.

DOI: [10.1103/PhysRevAccelBeams.26.103101](https://doi.org/10.1103/PhysRevAccelBeams.26.103101)

I. INTRODUCTION

Superconducting radio frequency (SRF) technology is central to delivering highly efficient particle beams in continuous wave or high duty cycle operation for basic science applications [1–12]. Further efficiency enhancement at moderate peak accelerating fields has been achieved by introducing impurities into Nb SRF cavities [13,14]. The N-doping process via thermal diffusion of N at 800 °C was chosen for production cavities in the LCLS-II and LCLS-II HE based on the reproducibility of the intended performance. During the LCLS-II HE research and development program, the performance of three N-doping protocols was investigated [15]. It was shown that the process of nitrogen doping Nb cavities at 800 °C for 2 min in an N₂ atmosphere with no postdope anneal was preferable to cavities doped for 2 min and annealed for 6 min or doped for 3 min and annealed for 60 min. After the nitrogen doping process, an electropolish is performed to recover performance by removing the acicular

nitrides [16] from the surface. Removal of nitrides via electropolishing is accompanied by roughening of the surface [17,18]. Recent investigations of 3-min doped cavities subjected to deeper electropolishing show improved maximum accelerating gradients [19].

Other surface treatments like nitrogen infusion [20] and oxide dissolution and oxygen diffusion have been shown to be efficacious in reducing surface resistance [21–23]. A benefit of these surface treatments is they do not require electropolishing after the heat treatment, reducing the number of process steps to achieve high performance [24], however, a vulnerability to form shallow carbides exists [20,25,26]. These carbides intrude into the surface as sharp needles which may cause a combination of local heating, trapping of vortices, and reduction of the local superheating field [27].

The smoothness of the inner surface of SRF cavities is one of the many important facets for achieving high performance SRF cavities. An ideal surface would be free of geometrical defects for the purpose of facilitating the largest possible peak magnetic field. Maximum peak magnetic fields may be suppressed via magnetic field enhancement (MFE) which results from supercurrent screening of magnetic fields by rough surfaces [28–31]. Magnetic field enhancements are greatest near sharp edges and increase with decreasing radius of curvature of the topographic defect [31,32]. At sufficiently high fields,

*lechner@jlab.org

Published by the American Physical Society under the terms of the *Creative Commons Attribution 4.0 International* license. Further distribution of this work must maintain attribution to the author(s) and the published article's title, journal citation, and DOI.

enhancement in the local magnetic field may turn regions of the defect normal conducting which expands and leads to thermal instabilities [28,33,34].

Nanoscale roughness may substantially alter the stability of the Meissner state [35–37]. Despite vortices being thermodynamically stable above B_{c1} , the Meissner state is metastable upto B_{sh} due to the existence of the Bean-Livingston barrier [38]. The barrier accounts for the competition between the force of the magnetic field pushing a vortex into the surface and the force from the surface expelling it. At B_{sh} , the surface is absolutely unstable to nucleation of highly dissipative vortices that may contribute to thermal instabilities [39,40]. The introduction of topographic defects enhances the force pushing the vortex into the surface and reduces the force from the surface, thereby reducing the superheating field [36].

Seeking to reduce the surface roughness, many techniques to polish the inner surface have been developed which help to achieve high accelerating fields [41–46]. Topographic characterization of SRF material subjected to these polishing techniques is often performed using atomic force microscopy (AFM), stylus profilometry, optical profilometry, or white light interferometry using samples or replicas [47]. In other studies, the power spectral density is often taken as a figure of merit for the surface finish [48–51], although it plays a little role in excess dissipation [52] for common SRF structures and its connection with ultimate peak magnetic field is not obvious. In this work, we examine the effect of electropolishing on the topography of heat-treated Nb and investigate the evolution of local magnetic field enhancement and superheating field suppression factors upon electropolishing.

II. EXPERIMENTAL

A. Scanning electron microscopy

The electron backscatter diffraction (EBSD) orientation image maps (OIM) related to sample preparation were obtained using an EDAX Velocity EBSD camera on a Tescan VEGA XMH3 scanning electron microscope (SEM) with a LaB_6 filament at Thomas Jefferson National Accelerator Facility. Additionally, high-resolution OIM were acquired on an EDAX EBSD velocity camera at the University of Utah. To best index the small particulate features, the EBSD was performed using 12 kV/1.6 nA beam conditions. To further improve the indexing of these small features, the EDAX software “OIM Matrix” was employed to improve the confidence index of these results.

B. Secondary ion mass spectrometry

Secondary ion mass spectrometry (SIMS) measurements were made using a CAMECA 7f Geo magnetic sector SIMS using a primary ion beam of Cs^+ with an impact energy of 8 keV (5 kV beam/−3 kV sample). The ion beam was rastered over an area of $150 \times 150 \mu\text{m}^2$ and the data collected from a $63 \times 63 \mu\text{m}^2$ area in the center of a

single grain. The relative sensitivity factors (RSF) for N were obtained by analyzing implant standards dosed with 2×10^{15} atoms/ cm^2 at 160 keV by Leonard Kroko Inc. The RSF values obtained were applied to the experimental results to convert the signal from counts to concentration (ppma).

C. Atomic force microscopy

Tapping-mode AFM topographies were acquired using a Digital Instruments Nanoscope IV atomic force microscope on loan to Thomas Jefferson National Accelerator Facility from The College of William and Mary. All measurements were acquired in tapping mode. Si AFM probes with a tip radius of less than 10 nm were used.

D. Sample preparation

All samples, including implant standards, were prepared from Tokyo Denkai Nb stock, residual resistivity ratio (RRR) ~ 300 , procured using the XFEL/007 specification [53]. The Nb samples were wire electrical discharge machined to size ($6 \times 10 \times 3 \text{ mm}^3$) from Nb stock. Subsequently, the samples were buffered chemical polished (BCP) using a 1:1:1 by volume mixture of hydrofluoric (49%), nitric (70%), and phosphoric acid (85%), respectively, removing 50 μm . Samples were then subjected to a vacuum heat treatment at 1000 °C for 1 h for grain growth. Following grain growth, samples were subjected to an additional 50- μm buffered chemical polish. Samples were then mechanically polished using a SiC abrasive followed by a 9- μm diamond suspension. The final polishing solution consists of colloidal silica (50 nm), H_2O_2 , and H_2O [54]. Using only colloidal silica produces a textured surface that reveals the grains as shown in Fig. 1(a).

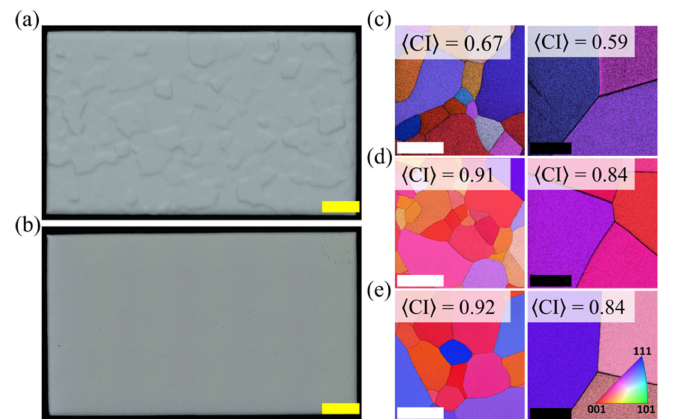


FIG. 1. (a) Optical microscope images showing the effect of H_2O_2 on mechanically polished Nb without and (b) with the addition of H_2O_2 , the yellow scale bar indicates 1 mm. The grain-textured surface returns if polished without H_2O_2 . (c–e) EBSD OIM of samples subjected to (c) no electropolishing, (d) 6- μm electropolishing, and (d) 20- μm electropolishing. The white and black scale bars indicate 350 and 16 μm , respectively.

The role of hydrogen peroxide in the solution is to suppress grain orientation dependent polishing as shown in Fig. 1(b). Mechanical polishing introduces superficial damage. Electron backscatter diffraction (EBSD) orientation image microscopy (OIM) was performed on mechanically polished samples showing relatively poor confidence indexing (CI) while an additional 6- μm electropolish increased the CI and 20- μm electropolishing did not further increase CI as shown in Figs. 1(c), 1(d), and 1(e). An electropolishing removal of 20 μm from the surface after mechanical polishing was selected as this has been efficacious after centrifugal barrel polishing for cavities [42]. More details about this chemical mechanical polishing process will be published elsewhere. All mechanical polishing was performed on an AutoMet 300.

Samples were hydrogen degassed at 600 °C for 10 h before further surface treatment. Intragrain average roughness, S_a , measured over a $50 \times 50 \mu\text{m}^2$ area using atomic force microscopy, is routinely less than 5 nm. During each heat treatment, samples were housed in a double-walled Nb foil container to minimize contamination from the furnace environment [55,56]. Further characterization of the mechanical polishing process described here will be published elsewhere.

III. RESULTS AND DISCUSSION

After sample preparation, samples were heat treated and then subjected to multiple rounds of electropolishing to investigate their topographic evolution. Electropolishing was performed using a 1 to 10 by volume mixture of HF (49%) to H_2SO_4 (98%). Samples of $6 \times 10 \times 3 \text{ mm}^3$ were wrapped in PTFE tape, mounted in a sample holder, and immersed in the electropolishing electrolyte allowing only the polished face to be exposed to the electrolyte. The current between anode and cathode was recorded using a digital multimeter and material removal was determined by utilizing Faraday's laws of electrolysis (five electrons per Nb atom removed) [57] and the controlled exposed surface area of each sample. Samples were electropolished at 13 °C and 9 V. The EP temperature is similar to that chosen for the cold EP process used in LCLS-II [58–60]. The voltage selected is based upon realizing the “plateau” I–V conditions without excessive heat generation for our bench electropolishing geometry. The samples investigated were subjected to vacuum annealing at 600 °C for 10 h, 300 °C for 3 h, and N-doped samples that were vacuum annealed at 800 °C for 3 h, exposed to a 20-mTorr N_2 atmosphere at 800 °C for 2 min with no postdope vacuum anneal and 6 min anneal at 800 °C, labeled 2N0 and 2N6, respectively, as well as samples N-doped at 800 °C for 3 min and vacuum annealed for 60 min, labeled 3N60. Two samples of each heat-treatment process were investigated with AFM. Three intragrain and three grain boundary triple junction topographies were acquired on each sample starting at 1 and 3 μm electropolishing depths, respectively. As shown in

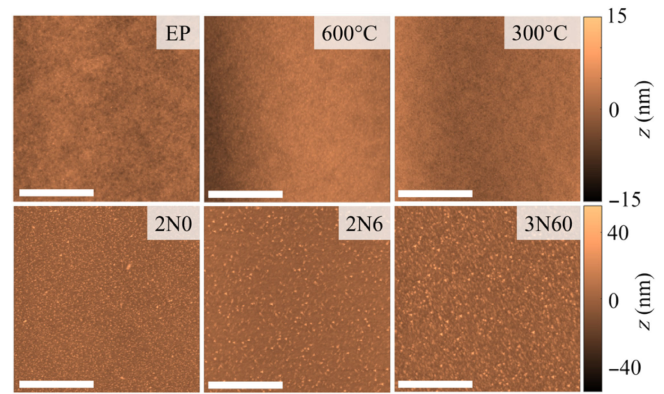


FIG. 2. Representative tapping-mode AFM topographies of the heat-treated surfaces. The topography labeled EP is representative of a sample heat treated at 600 °C for 10 h then subjected to a 20- μm electropolish, the sample labeled 600 °C is representative of a sample heat treated at 600 °C for 10 h without postanneal electropolish. The topography labeled 300 °C is representative of a sample heat treated at 300 °C for 3 h and the topographies labeled 2N0, 2N6, and 3N60 are N doped as described in the text, all without post-heat-treatment electropolishing. Scale bars are 10 μm .

Fig. 2, the heat-treated surfaces of samples subjected to 600 and 300 °C are similar to that of the electropolished (EP) surface. The N-doped surfaces have nitride precipitates scattered across its surface.

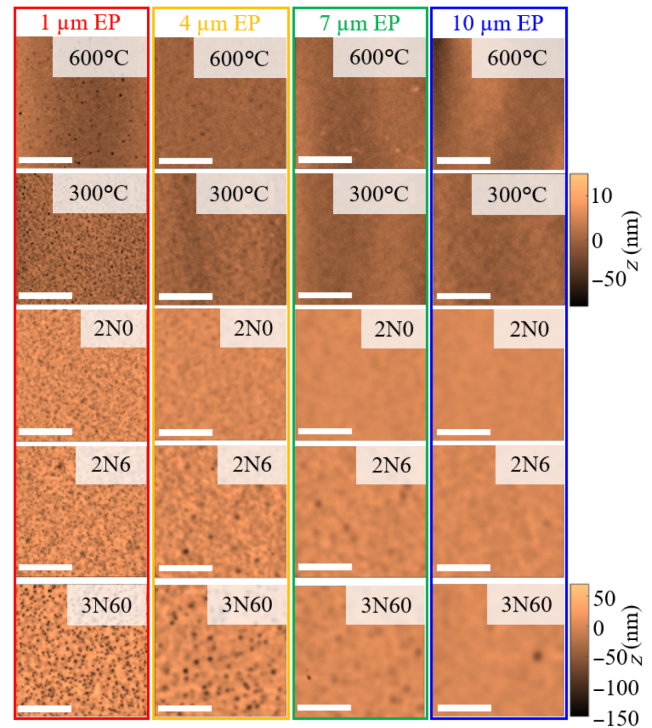


FIG. 3. Representative tapping-mode AFM topographies of the heat-treated surfaces after electropolishing within grains. Note the difference in scales between the vacuum-annealed and N-doped samples. Scale bars are 10 μm .

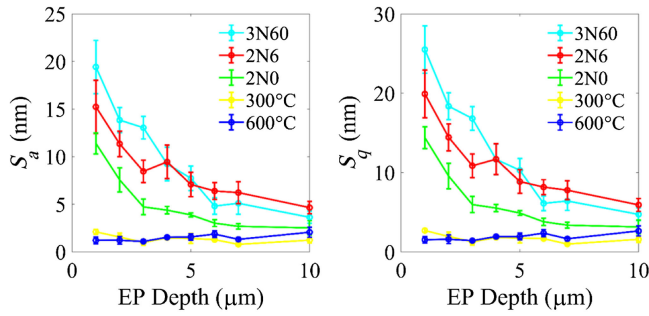


FIG. 4. Evolution of the average surface roughness, S_a , and rms roughness, S_q , from the tapping-mode AFM topographies of the as heat-treated surfaces within a grain. Pre-EP, $S_a \leq 5$ nm for the 600 and 300 °C heat-treated samples, while $S_a \leq 10$ nm for the N-doped samples. The increase in S_a for the N-doped samples is due to the formation of nitrides.

Upon electropolishing the samples of 1 μm , all sample surfaces show roughening within grains, this effect is pronounced in the N-doped samples where holes are formed as shown in Fig. 3 and consistent with previous work [17]. We speculate that roughening observed in the 600 °C heat-treated samples may be due to a phenomenon similar to the N-doped case where a shallow niobium carbide phase may develop [20,25,26,61]. The roughness reduces upon the progression of electropolishing as shown in Fig. 3. The average intragrain roughness substantially decreases with the progression of electropolishing for the N-doped samples while the 300 and 600 °C heat-treated samples retain their comparatively low roughness as shown in Fig. 4.

The origin of the holes in the N-doped surfaces is due to the electropolishing of this two-phase system. This effect is most pronounced at grain boundaries where nitrides can precipitate continuously along it as shown in Figs. 5(a) and 5(b). Cross sections show that the nitrides extend toward the bulk with a sharp interface between the two phases as shown in Fig. 5(c).

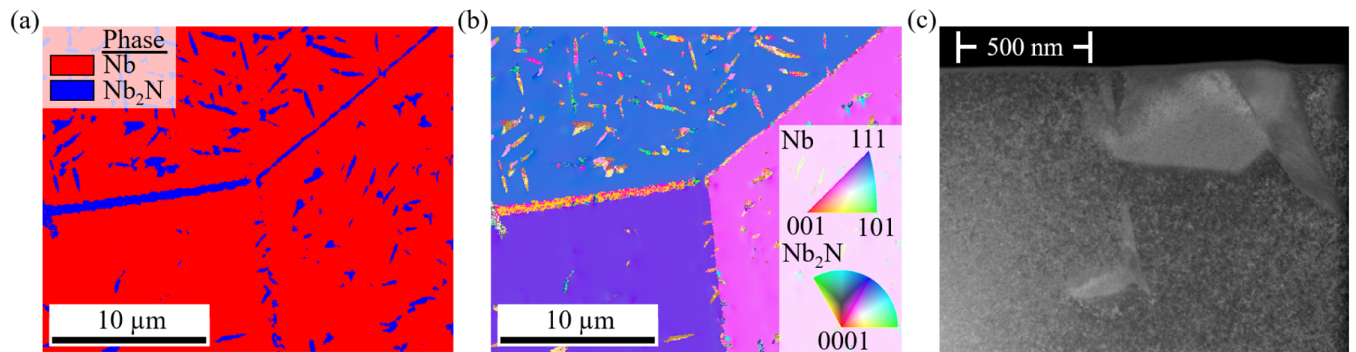


FIG. 5. (a) Phase map and (b) orientation map of a 2N0 N-doped sample showing the formation of Nb nitrides within grains and along grain boundaries. (c) Scanning transmission electron micrograph of a 3N60 N-doped Nb sample showing the formation of sharp Nb nitrides that intrude into the surface. All N-doped recipes investigated in this work produce qualitatively similar surfaces with nitrides forming within grains and along grain boundaries.

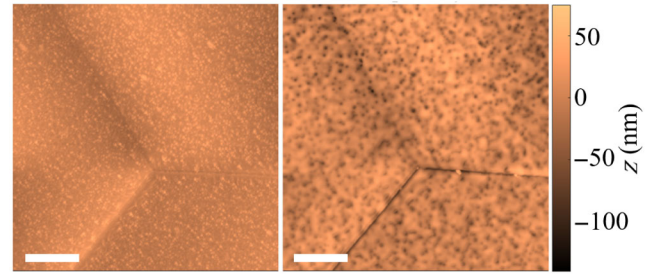


FIG. 6. Tapping-mode AFM topographies of the native surface of an as-treated 2N0 sample (left) and after 1 μm surface removal via electropolishing (right). After electropolishing grooves develop along grain boundaries. The scale bar is 5 μm .

Upon electropolishing, the nitrides are preferentially attacked and leave behind holes as shown in the tapping-mode atomic force microscope maps before and after a 1- μm electropolish shown in Fig. 6. Grain boundaries are the most systematically affected since the nitrides preferentially precipitate along them. Representative tapping-mode AFM topographies of grain boundaries after sequential electropolishing are shown in Fig. 7. The grooves produced by the N-doping and electropolishing process tend to become less severe with greater electropolishing depths. The persistence of these extended defects along grain boundaries appears less severe in the 2N0 samples. Another common defect, characterized by particularly deep holes, is formed at grain boundary triple junctions. This behavior is likely due primarily to enhanced diffusion at grain boundaries and is most severe in the 3N60 samples.

An extended grain boundary groove oriented along the direction of the magnetic field is reminiscent of the long triangular groove defect studied theoretically by Kubo [36] where nanoscale topographic features may decrease the superheating field. Kubo's model predicts a superheating field suppression factor based on simple geometric features of the surface and the superconductor's coherence length. The model is defined by the triangular groove slope

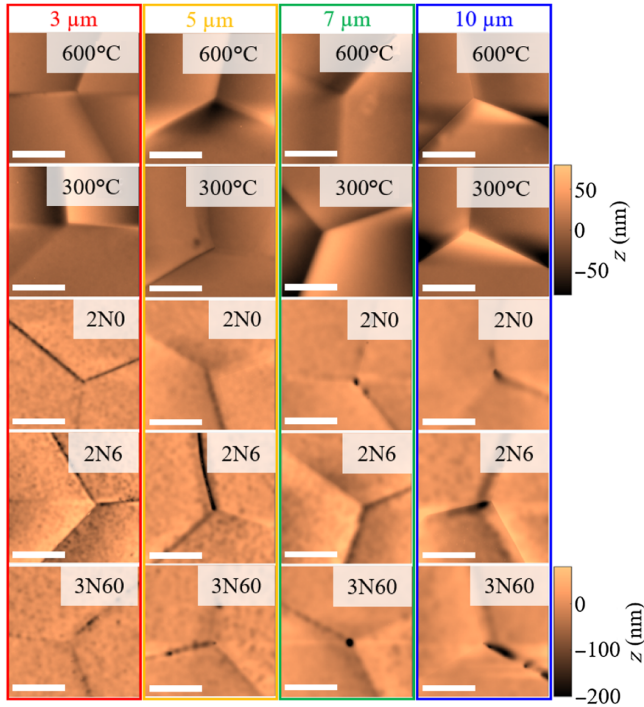


FIG. 7. Representative tapping-mode AFM topographies of the heat-treated surfaces within a grain. Note the difference in color scales between the vacuum-annealed and N-doped samples. Scale bars are 10 μm .

angle, θ , depth of the groove, δ , and the coherence length, ξ . The superheating field suppression factor, η , defined from $\tilde{B}_s = \eta B_s$ is calculated by

$$\eta = \frac{1}{\alpha} \left(\frac{(\Gamma(\frac{\alpha}{2}))\Gamma(\frac{3-\alpha}{2})\alpha \sin(\frac{\pi(\alpha-1)}{2})}{\sqrt{\pi}} \frac{\xi}{\delta} \right)^{\frac{\alpha-1}{\alpha}}, \quad (1)$$

where $\theta = \pi(\alpha - 1)/2$. Evaluating η using topographic information requires an estimation of the local slope angle and depth of the groove. Assuming an implicit surface defined by $F = z - h(x, y) = 0$, the local slope angle is given by

$$\cos \theta = \hat{\mathbf{z}} \cdot \hat{\mathbf{n}} = \hat{\mathbf{z}} \cdot \frac{(-h_x, -h_y, 1)}{(1 + h_x^2 + h_y^2)^{\frac{1}{2}}}, \quad (2)$$

where $\hat{\mathbf{n}}$ is the unit normal vector to the measured surface, h_i is the partial derivative of h with respect to coordinate i [62]. Partial derivatives of $h(x, y)$ were calculated using an extension of the Savitzky-Golay filtering method for surfaces [63,64]. To estimate the depth of the holes and grooves, we define $\delta(\mathbf{r})$ as the difference between the AFM topography and a fitted plane that conforms to the surface without conforming to the holes and defects. For the 600 $^{\circ}\text{C}$ heat-treated Nb, we estimate the material to be clean and assign $\xi = 39$ nm [65]. We use $\xi = 28$ nm in the N-doped

and 300 $^{\circ}\text{C}$ heat-treated Nb based on rf measurements that indicate an average electron mean free path $l \approx 100$ nm [22,66] and utilizing $\xi^{-1} = \xi_0^{-1} + l^{-1}$ [67] where ξ_0 is the clean limit coherence length.

While the entrance of vortices should occur at the valley minima, the grain boundary grooves present slope angles that are not constant throughout and often the grooves observed have depths comparable to the length scale of the penetration depth which deviates from Kubo's model assumptions. With these limitations in mind, we utilize Eq. (1) using $\alpha(\mathbf{r})$, ξ and $\delta(\mathbf{r})$ to calculate $\eta(\mathbf{r})$. We note that $\eta(\mathbf{r})$ does not represent a local superheating field suppression factor except in some cases near minima. A representative topography, slope angle map, slope angle histogram, and $\eta(\mathbf{r})$ map are shown for a 2N6 sample after 3 μm of electropolishing in Fig. 8.

To examine the evolution of the magnetic field enhancement factor, $\beta(\mathbf{r})$, we utilized AFM topographies [Fig. 9(a)] and modeled the surface as a perfect electrical conductor. In the absence of free currents and a static magnetic field, a magnetic scalar potential, ψ , can be employed and is governed by Laplace's equation $\nabla^2 \psi = 0$. We modeled the magnetic field, $\mathbf{B}(\mathbf{r}) = B_0 \hat{x}$ far from the surface which allows a magnetic scalar potential $\psi = -B_0 x$. Faces were assigned the following boundary conditions $\nabla \psi \cdot \hat{x} = B_0$, $\nabla \psi \cdot \hat{y} = 0$, and $\nabla \psi \cdot \hat{n} = 0$ for the sample's surface. Opposing and far above the sample's surface, $\psi(x, y, z_{\text{max}} = 6 \mu\text{m}) = -B_0 x$. The partial differential equation was solved via finite element analysis using MATLAB 2022a's Partial Differential Equation Toolbox. Node to node distances were set to 50 nm at the sample's surface as shown in Fig. 9(b). The magnetic field enhancement factor at the sample's surface

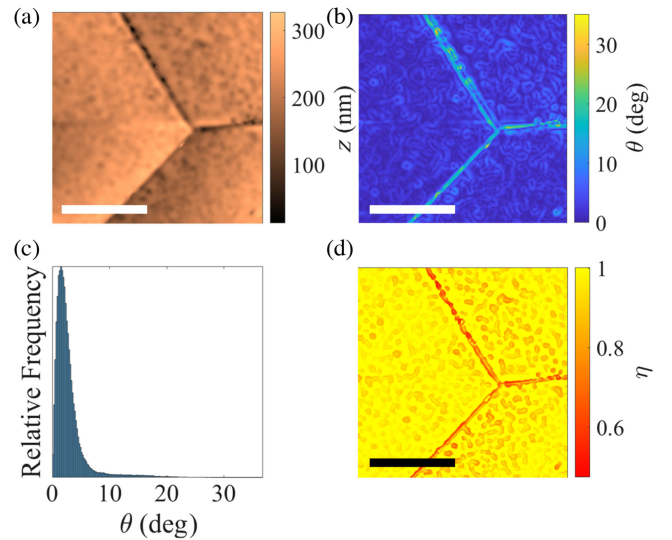


FIG. 8. (a) Representative AFM topography, (b) local slope angle, θ , (c) slope angle histogram, and (d) $\eta(\mathbf{r})$ for a 2N6 sample after 3- μm surface removal via electropolishing. Scale bars are 10 μm .

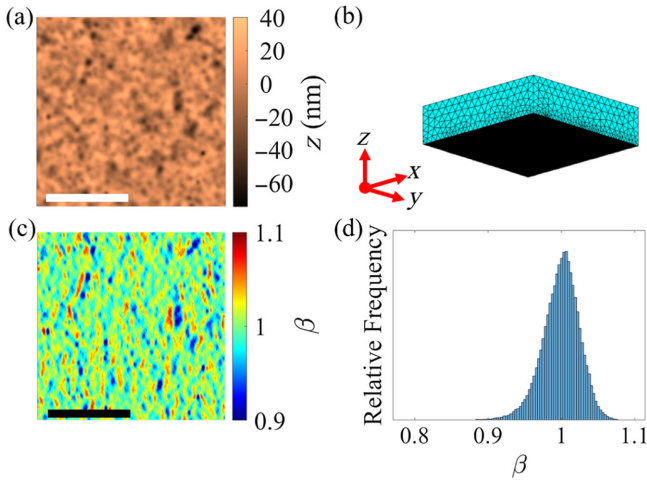


FIG. 9. (a) Tapping-mode AFM topography of a 2N6 sample after 3 μm of electropolishing used to construct the model mesh. (b) Mesh used for the solution of the magnetic scalar potential. (c) Local magnetic field enhancement factor at the surface. (d) Histogram of magnetic field enhancement factors. Scale bars are 10 μm .

was computed as $\beta(\mathbf{r}) = |\mathbf{B}(\mathbf{r})|/B_0$ plotted in Fig. 9(c) and their relative frequency in Fig. 9(d). Simulating at smaller length scales requires more complex methods of solution [40].

$\eta(\mathbf{r})$ was examined by heat treatment process and electropolishing depth as shown in Fig. 10. Representative triple junction $\eta(\mathbf{r})$ maps are shown in Fig. 10(a) and their frequency of occurrence is plotted in Fig. 10(b). The relative frequency of η for intragranular topographies is shown in Fig. 10(c). Relative frequencies of 10^{-4} or greater are of significance based on the area sampled with the AFM. 10^{-4} corresponds to an area of $650 \times 650 \text{ nm}^2$ which in turn corresponds to approximately the size of a whole defect in this system. Choosing smaller relative frequencies corresponds to subdefect regions which may sample low $\eta(\mathbf{r})$ that are not constant throughout the defect and choosing larger ones ignores small complete defects. In both the triple junction and intragrain areas, the N-doped samples show a clear degradation of the superheating field suppression factor due to the development of sharp grooves at the grain boundaries. A clear trend is observed that the electropolishing substantially eliminates low $\eta(\mathbf{r})$ values during electropolishing in N-doped material, while little improvement is observed in the 600 and 300 $^\circ\text{C}$ heat-treated samples. In the intragrain histograms, the 3N60 and 2N6 samples show the worst developments of low $\eta(\mathbf{r})$ values. Similarly, the 2N6 process presents more severe $\eta(\mathbf{r})$ values compared with the 2N0 process, with the 3N60 showing some rare, low- $\eta(\mathbf{r})$. During electropolishing, there is improvement in low $\eta(\mathbf{r})$ values but substantial degradation in the superheating field suppression factor persists into 10 μm total removal in the N-doped samples.

Representative magnetic field enhancement factors at grain boundaries are shown in Fig. 11(a). The vacuum-annealed samples show the least magnetic field enhancement inter/intragranularly while the N-doped samples show the largest enhancements with the 3N60 samples showing the highest spread. The relative frequency of MFE factors was investigated with increasing electropolishing depth for the intragrain [Fig. 11(b)] and triple junction, Fig. 11(c) tapping-mode AFM topographies. Intragranularly and intergranularly, the progression of the MFE factors shows a general trend of converging toward unity with electropolishing. Magnetic field enhancement is greatest in the N-doped samples due to the holes left behind from the nitride precipitation and electropolishing process which is seen most clearly in the intragrain images. However, in the triple junction images, step heights are the dominating contribution to magnetic field enhancement. Among the N-doped samples, the 2N6 and 3N60 processes appear to have the most severe MFE factors intragranularly and intergranularly. The 300 and 600 $^\circ\text{C}$ heat-treated samples have the least severe magnetic field enhancement intragranularly or intergranularly. Both intergranularly or intragranularly MFEs show ~ 1.2 or better across all samples after 3- μm electropolishing.

In alloyed superconductors, a decrease in the depairing current density may be expected in dirtier material [68]. We examined N impurity concentration profiles of three N-doping processes using secondary ion mass spectrometry as shown in Fig. 12. SIMS method sensitivities and vulnerabilities in Nb have recently been explored and refined with measurement errors approaching $\sim 10\%$ [56,69–72]. We find that all concentration profiles show a similar concentration of N introduced, between 600 and 900 ppma, into the first $\sim 10 \mu\text{m}$. The intended electropolishing depth for the 2N6 process was 5-7 μm [15] and 7 μm for the 2N0. The difference in N concentration at the surface between the 2N0 and 2N6 processes is small and shows no measurable difference in surface resistance [73] indicating a negligible difference in electron mean free path between these processes. A gain of $\sim 5 \text{ MV/m}$ [73,74] in average maximum accelerating gradient, from 22 to 27 MV/m, cannot be accounted for by expected changes in the superheating field due to changes in mean free path and may instead come from improvements in the nature of topographic defects. In Fig. 13, we compare the 2N6 and 2N0 η distributions finding $\eta_{\min} = 0.61$ and 0.76, respectively. To estimate the difference in the expected maximum accelerating field in TESLA-shaped cavities (4.24 mT/MV) [75], we consider the ideal superheating field of a perfectly flat dirty Nb as 160 mT [76] and obtain 23 and 29 MV/m in approximate agreement with the improvement observed. When compared with the MFE distributions, a value of ~ 1.2 yields a maximum accelerating gradient of 31 MV/m. This suggests that the reduction of the superheating field suppression due to

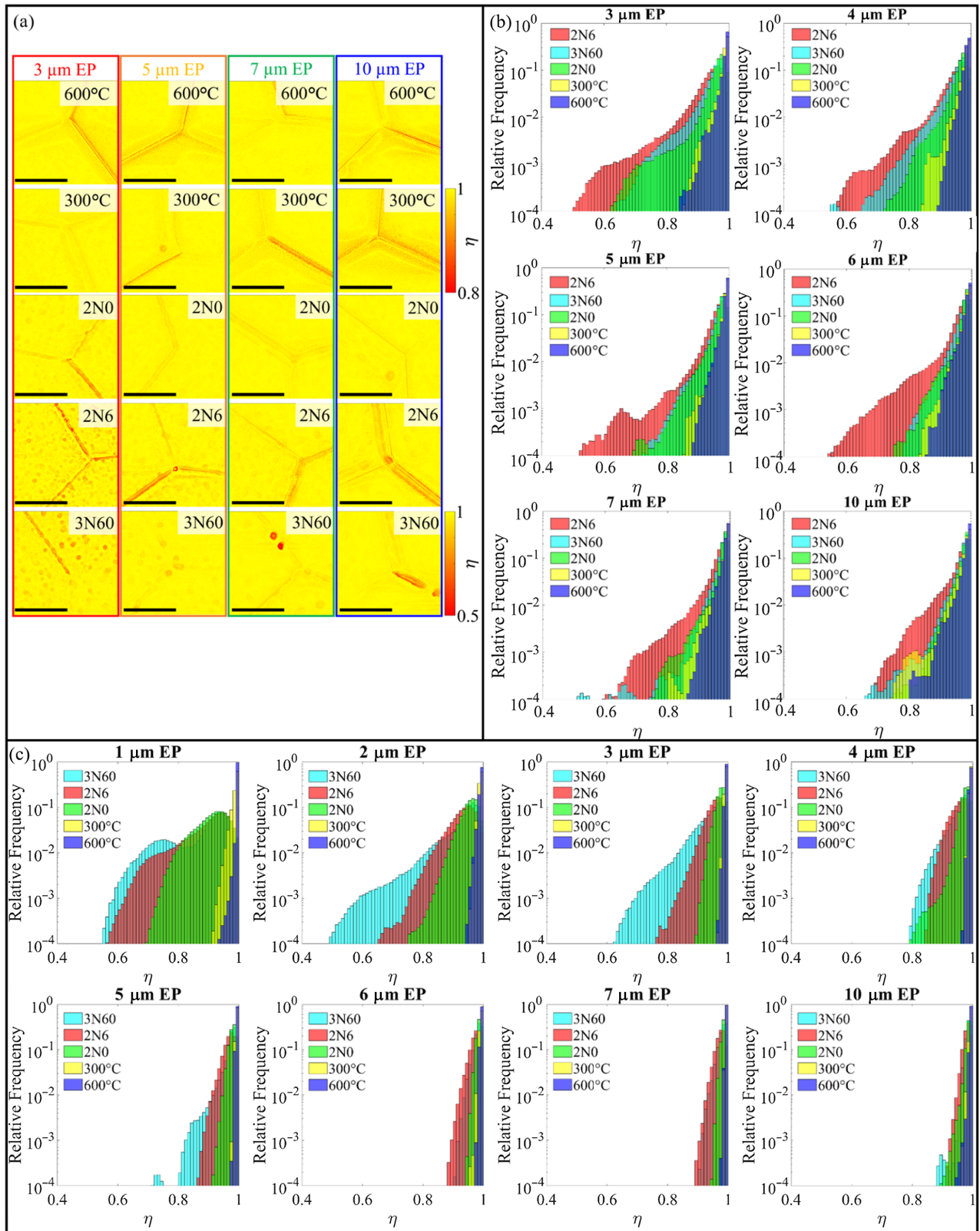


FIG. 10. (a) Representative triple junction η maps upon electropolishing. Scale bars are 10 μm . (b) Evolution of intragrain $\eta(\mathbf{r})$ histograms upon electropolishing. (c) Evolution of triple junction $\eta(\mathbf{r})$ histograms upon electropolishing.

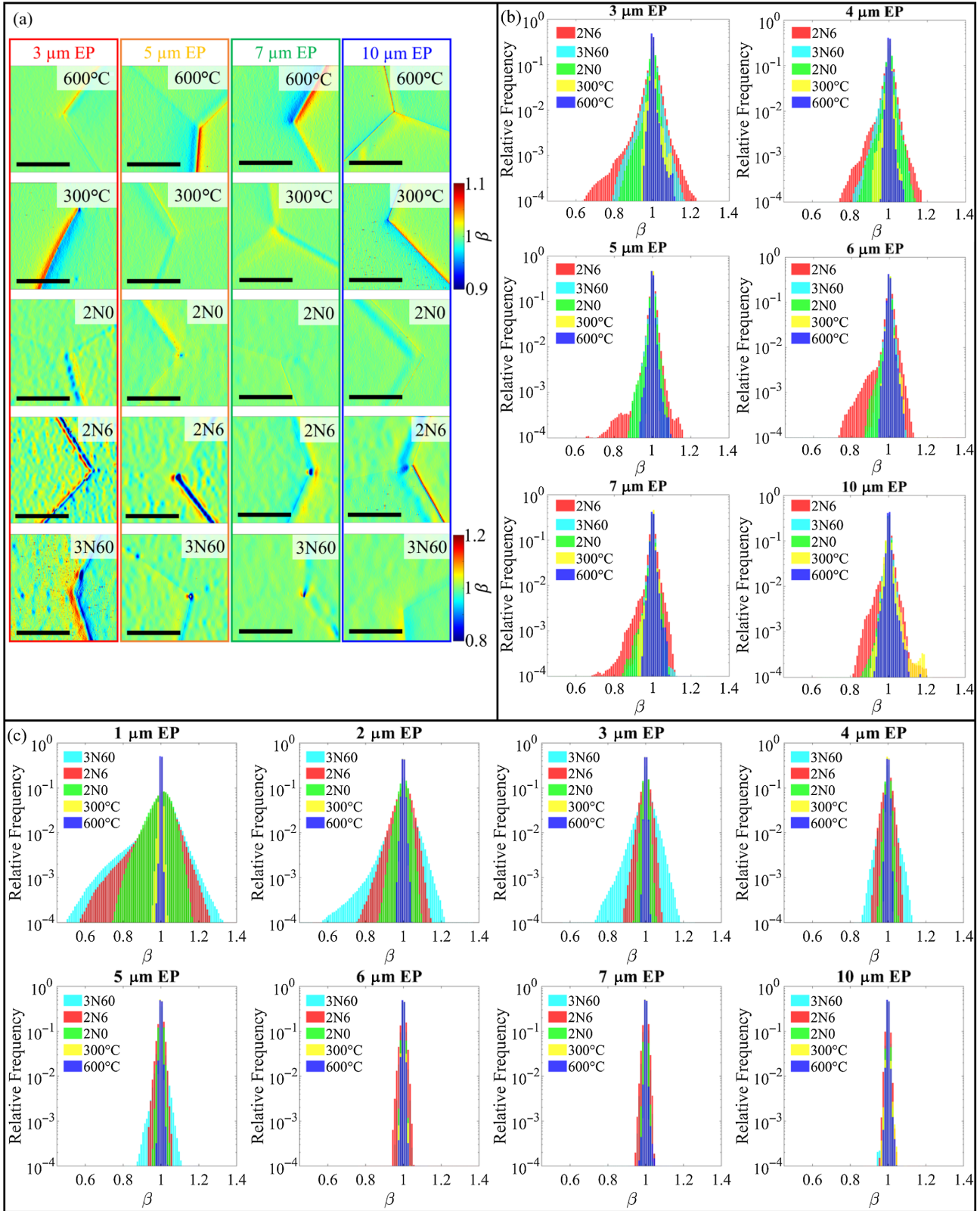


FIG. 11. (a) Representative evolution of triple junction $\beta(\mathbf{r})$ maps upon electropolishing. Scale bars are 10 μm . (b) Evolution of intragrain $\beta(\mathbf{r})$ histograms upon electropolishing. (c) Evolution of triple junction $\beta(\mathbf{r})$ histograms upon electropolishing.

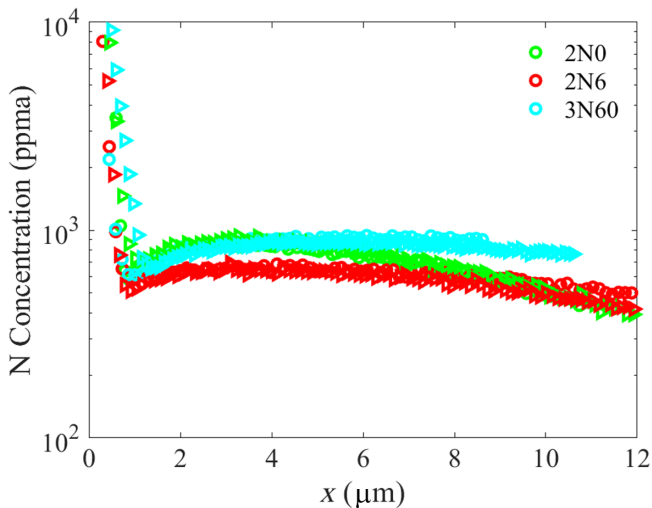


FIG. 12. SIMS depth profile of N impurities in 2N0, 2N6, and 3N60 samples.

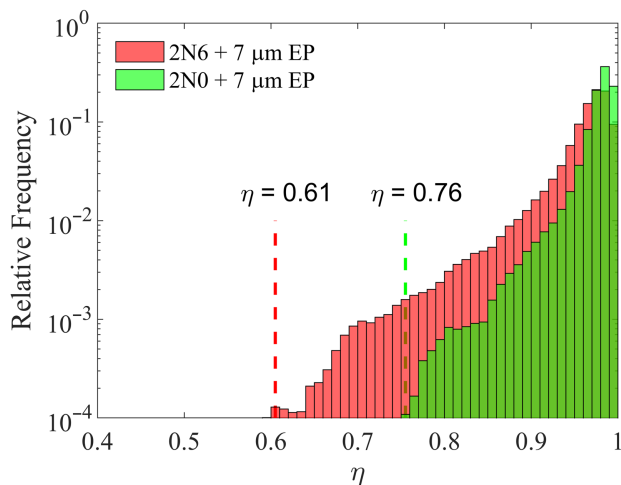


FIG. 13. Comparison of η between the 2N0 and 2N6 processes.

triangular grooves is dominant in 2N6 recipes while MFE and superheating field suppression are more comparable for the 2N0 process, but superheating field suppression via triangular grooves remains slightly more prominent. If magnetic field enhancement and superheating field suppression are to coincide, at a grain boundary triple junction exhibiting a step and a groove for example, using an average MFE factor of ~ 1.1 , one may expect a further reduction to 21 and 26 MV/m for the 2N6 and 2N0 recipes.

This tends to indicate that the main differences in the quench field between the three protocols investigated in the LCLS-II HE R&D program [15] may not be primarily associated with interstitial impurity content but rather by the roughening of the surface and growth of phases into the surface. This is consistent with the observation that with

increased electropolishing depths to 10 μm , the 3N60 process has exhibited high performance comparable to the 2N0 process [19,77]. The 300 $^{\circ}\text{C}$ heat treatment tends to exhibit improved η which may facilitate larger accelerating fields than N-doped cavities. This observation is consistent with rf measurements of 1.3-GHz single-cell cavities heat treated between 250 and 400 $^{\circ}\text{C}$ [24].

IV. CONCLUSIONS

Nb samples subjected to typical SRF cavity heat treatments have been investigated with SEM, SIMS, and sequentially electropolished samples by AFM. Nitrides form within grains and continuously along some grain boundaries. For N-doped Nb, nitrides are observed to be preferentially attacked and removed during electropolishing which leaves behind a topographically imperfect surface marked by holes and grooves along grain boundaries. During electropolishing minor changes in magnetic field enhancement and superheating field suppression factors are observed for the 300 and 600 $^{\circ}\text{C}$ heat-treated Nb, while substantial improvements are observed for N-doped Nb. After a few-micrometer electropolish, between magnetic field enhancement factors and superheating field suppression factors, we find that the most severe defects in N-doped Nb are the grain boundary grooves. Magnetic field enhancement tends to be a comparatively minor contributor to the reduction of peak accelerating fields in N-doped material until larger electropolishing removals are achieved.

The severity of topographic defects in N-doped Nb is dependent on the N-doping process. The distribution of magnetic field enhancement factors and superheating field suppression factors supports the hypothesis that shorter annealing and N_2 exposures tend to reduce the surface roughness for N-doped Nb. From the topographs, samples that underwent the 3N60 and 2N6 heat treatments have nitrides extending further into the bulk likely due to Ostwald ripening of the Nb_2N phase during the extended anneal. Our results may indicate that the improvement in the N-doping protocol used in the LCLS-II HE SRF cavity production may come from the improved smoothness at grain boundaries for the applied amount of electropolishing removal.

Theoretical studies [35,36] clearly show that as a material moves deeper into the type-II regime, it becomes substantially more sensitive to Bean-Livingston barrier breakdown due to topographic defects. Special care should be paid to the surface roughness of alloyed cavities for high-field operation. Ideally, after N-doping, a long electropolish to remove the topographic defects would be employed, however, this must coincide with elevated N content within the rf active region. Diffusion lengths are not long enough to accommodate this in the 2N6 and 2N0 processes. Processes like 3N60 offer longer impurity profiles and also rougher surfaces, which must be

electropolished deeper. Longer impurity diffusion profiles that change negligibly in concentration during electro-polishing would be preferable to negate the effects of topographic defects introduced during heat treatments. Obtaining the same low surface resistance and high accelerating fields after heat treatment, without additional electropolishing, is ideal. This can be achieved with the oxide dissolution and oxygen diffusion processes, which hold the potential to maintain peak magnetic fields at ~ 30 MV/m or higher depending on smoothness but may be sensitive to shallow carbide formation [25].

The analysis methods developed herein utilized measured topographs to simulate magnetic field enhancement and estimate local suppressions of the superheating field. These analysis methods will be useful for improving surfaces or polishing processes of interest for SRF applications where roughness is more severe or where the ultimate performance may be sensitive to topographic defects [36,78–81].

ACKNOWLEDGMENTS

This was coauthored by Jefferson Science Associates, LLC under U.S. DOE Contract No. DE-AC05-06OR23177. This material is based on the work supported by the U.S. Department of Science, Office of Science, Office of Nuclear Physics Early Career Award to A. Palczewski. The authors are grateful for the support from the Office of High Energy Physics, U.S. Department of Energy under Grant No. DE-SC-0018918 to Virginia Tech for the support of J. W. A. We gratefully acknowledge O. Trofimova for some of the SEM measurements presented here, G. Ciovati for fruitful discussions, and R. Overton and T. Harris for support in sample preparation.

[1] H. S. Padamsee, *Annu. Rev. Nucl. Part. Sci.* **64**, 175 (2014).
 [2] C. W. Leemann, D. R. Douglas, and G. A. Krafft, *Annu. Rev. Nucl. Part. Sci.* **51**, 413 (2001).
 [3] J. Rossbach, *Nucl. Instrum. Methods Phys. Res., Sect. A* **375**, 269 (1996).
 [4] C. Bostedt, S. Boutet, D. M. Fritz, Z. Huang, H. J. Lee, H. T. Lemke, A. Robert, W. F. Schlotter, J. J. Turner, and G. J. Williams, *Rev. Mod. Phys.* **88**, 015007 (2016).
 [5] M. Altarelli, R. Brinkmann, and M. Chergui, The European X-ray free-electron laser, Technical design report, DESY Technical Report No. DESY-06-097, 2007.
 [6] S. Henderson, W. Abraham, A. Aleksandrov, C. Allen, J. Alonso, D. Anderson, D. Arenius, T. Arthur, S. Assadi, J. Ayers *et al.*, *Nucl. Instrum. Methods Phys. Res., Sect. A* **763**, 610 (2014).
 [7] G. Bollen, *AIP Conf. Proc.* **1224**, 432 (2010).
 [8] V. Lebedev, The PIP-II reference design report, Fermi National Accelerator Laboratory Technical Report No. FERMILAB-DESIGN-2015-01, 2015.

[9] M. Lindroos, S. Bousson, R. Calaga, H. Danared, G. Devanz, R. Duperrier, J. Eguia, M. Eshraqi, S. Gammino, H. Hahn *et al.*, *Nucl. Instrum. Methods Phys. Res., Sect. B* **269**, 3258 (2011).
 [10] D. Jeon, I.-S. Hong, H. J. Kim, J. W. Kim, R. Bodenstern, H. J. Cha, S.-J. Choi, S. Choi, O. Choi, H. Do *et al.*, *J. Korean Phys. Soc.* **65**, 1010 (2014).
 [11] N. Phinney, N. Toge, and N. Walker, [arXiv:0712.2361](https://arxiv.org/abs/0712.2361).
 [12] C. E. Reece, *Phys. Rev. Accel. Beams* **19**, 124801 (2016).
 [13] P. Dhakal, G. Ciovati, G. R. Myneni, K. E. Gray, N. Groll, P. Maheshwari, D. M. McRae, R. Pike, T. Proslie, F. Stevie, R. P. Walsh, Q. Yang, and J. Zasadzinski, *Phys. Rev. ST Accel. Beams* **16**, 042001 (2013).
 [14] A. Grassellino, A. Romanenko, D. Sergatskov, O. Melnychuk, Y. Trenikhina, A. Crawford, A. Rowe, M. Wong, T. Khabiboulline, and F. Barkov, *Supercond. Sci. Technol.* **26**, 102001 (2013).
 [15] D. Gonnella, S. Aderhold, D. Bafia, A. Burrill, M. Checchin, M. Ge, A. Grassellino, G. Hays, M. Liepe, M. Martinello *et al.*, in *Proceedings of 19th International Conference on RF Superconductivity, SRF'19, Dresden, Germany* (JACoW, Geneva, Switzerland, 2019), 10.18429/JACoW-SRF2019-MOP045.
 [16] Y. Trenikhina, A. Grassellino, O. Melnychuk, and A. Romanenko, in *Proceedings of SRF2015, Whistler, BC, Canada* (JACoW, Geneva, Switzerland, 2015), p. 223.
 [17] J. Spradlin, A. Palczewski, H. Tian, and C. Reece, in *Proceedings of 19th International Conference on RF Superconductivity, SRF'19, Dresden, Germany* (JACoW, Geneva, Switzerland, 2019), p. 106.
 [18] P. Dhakal, G. Ciovati, U. Pudasaini, S. Chetri, S. Balachandran, and P. J. Lee, *Phys. Rev. Accel. Beams* **22**, 122002 (2019).
 [19] Y. Zong, Q. Chen, X. Huang, Z. Wang, J. Chen, P. Dong, H. Hou, X. Pu, J. Shi, S. Sun *et al.*, in *Proceedings of SRF'23* (JACoW Publishing, Geneva, Switzerland, 2023).
 [20] A. Grassellino, A. Romanenko, Y. Trenikhina, M. Checchin, M. Martinello, O. S. Melnychuk, S. Chandrasekaran, D. A. Sergatskov, S. Posen, A. C. Crawford, S. Aderhold, and D. Bice, *Supercond. Sci. Technol.* **30**, 094004 (2017).
 [21] F. Palmer, *IEEE Trans. Magn.* **23**, 1617 (1987).
 [22] S. Posen, A. Romanenko, A. Grassellino, O. Melnychuk, and D. Sergatskov, *Phys. Rev. Appl.* **13**, 014024 (2020).
 [23] E. M. Lechner, J. W. Angle, F. A. Stevie, M. J. Kelley, C. E. Reece, and A. D. Palczewski, *Appl. Phys. Lett.* **119**, 082601 (2021).
 [24] F. He, W. Pan, P. Sha, J. Zhai, Z. Mi, X. Dai, S. Jin, Z. Zhang, C. Dong, B. Liu, H. Zhao, R. Ge, J. Zhao, Z. Mu, L. Du, L. Sun, L. Zhang, C. Yang, and X. Zheng, *Supercond. Sci. Technol.* **34**, 095005 (2021).
 [25] H. Kimura and Y. Sasaki, *Trans. Jpn. Inst. Met.* **2**, 98 (1961).
 [26] A. Danguwal Pandey, T. F. Keller, M. Wenskat, A. Jeromin, S. Kulkarni, H. Noei, V. Vonk, W. Hillert, D. Reschke, N. Walker *et al.*, *Appl. Phys. Lett.* **119**, 194102 (2021).
 [27] A. Gurevich, *Supercond. Sci. Technol.* **30**, 034004 (2017).
 [28] J. Knobloch, R. Geng, M. Liepe, and H. Padamsee, in *Proceedings of the 1999 Workshop on RF Superconductivity, La Fonda Hotel, Santa Fe, NM* (CERN, Geneva, Switzerland, 1999), p. 77.

- [29] C. Xu, C. E. Reece, and M. J. Kelley, *Phys. Rev. Accel. Beams* **19**, 033501 (2016).
- [30] A. Gurevich, *Physica (Amsterdam)* **441C**, 38 (2006).
- [31] T. Kubo, *Prog. Theor. Exp. Phys.* **2015**, 073G01 (2015).
- [32] V. Shemelin and H. Padamsee, DESY TTC-Report No. 7, 2008.
- [33] Y. Xie, M. Liepe, and H. Padamsee, in *Proceedings of SRF2011, Chicago, IL* (CERN, Geneva, Switzerland, 2011), p. 687.
- [34] Y. Xie and M. Liepe, in *Proceedings of 16th International Conference on RF Superconductivity, SRF'13, Paris, France* (JACoW, Geneva, Switzerland, 2013), p. 378.
- [35] A. Aladyshkin, A. Mel'nikov, I. Shereshevsky, and I. Tokman, *Physica (Amsterdam)* **361C**, 67 (2001).
- [36] T. Kubo, *Prog. Theor. Exp. Phys.* **2015**, 063G01 (2015).
- [37] A. R. Pack, J. Carlson, S. Wadsworth, and M. K. Transtrum, *Phys. Rev. B* **101**, 144504 (2020).
- [38] C. P. Bean and J. D. Livingston, *Phys. Rev. Lett.* **12**, 14 (1964).
- [39] A. Gurevich and G. Ciovati, *Phys. Rev. B* **77**, 104501 (2008).
- [40] A. Gurevich, *Rev. Accel. Sci. Technol.* **05**, 119 (2012).
- [41] T. Higuchi, K. Saito, S. Noguchi, M. Ono, E. Kako, T. Shishido, Y. Funahashi, H. Inoue, and T. Suzukim, in *Proc. SRF'95* (CERN, Geneva, Switzerland, 1995), p. 723.
- [42] C. Cooper, K. Saito, B. Bullock, S. Joshi, and A. Palczewski, in *Proceedings of SRF2011, Chicago, IL* (CERN, Geneva, Switzerland, 2011), p. 571.
- [43] C. A. Cooper and L. D. Cooley, *Supercond. Sci. Technol.* **26**, 015011 (2012).
- [44] H. Tian, C. E. Reece, M. J. Kelley, S. Wang, L. Plucinski, K. E. Smith, and M. M. Nowell, *Appl. Surf. Sci.* **253**, 1236 (2006).
- [45] L. Zhao, J. M. Klopff, C. E. Reece, and M. J. Kelley, *Phys. Rev. ST Accel. Beams* **17**, 083502 (2014).
- [46] H. Tian, B. Straka, J. Carroll, C. Reece, T. Hall, R. Radhakrishna, M. Inman, and E. Taylor, in *Proceedings of 29th Linear Accelerator Conference, LINAC-2018, Beijing, China* (JACoW, Geneva, Switzerland, 2018), p. 431.
- [47] C. Xu, C. Reece, and M. Kelley, *Appl. Surf. Sci.* **274**, 15 (2013).
- [48] C. Xu, H. Tian, C. E. Reece, and M. J. Kelley, *Phys. Rev. ST Accel. Beams* **14**, 123501 (2011).
- [49] H. Tian, G. Ribeill, C. Xu, C. E. Reece, and M. J. Kelley, *Appl. Surf. Sci.* **257**, 4781 (2011).
- [50] C. Xu, H. Tian, C. E. Reece, and M. J. Kelley, *Phys. Rev. ST Accel. Beams* **15**, 043502 (2012).
- [51] U. Pudasaini, G. V. Eremeev, C. E. Reece, J. Tuggle, and M. J. Kelley, *Supercond. Sci. Technol.* **33**, 045012 (2020).
- [52] C. Xu, C. E. Reece, M. J. Kelley, and P. Takacs, *Nucl. Instrum. Methods Phys. Res., Sect. A* **904**, 124 (2018).
- [53] W. Singer, X. Singer, A. Brinkmann, J. Iversen, A. Matheisen, A. Navitski, Y. Tamashevich, P. Michelato, and L. Monaco, *Supercond. Sci. Technol.* **28**, 085014 (2015).
- [54] G. F. Vander Voort, *Pract. Metallogr.* **48**, 527 (2011).
- [55] A. Grassellino, A. Romanenko, A. Crawford, O. Melnychuk, A. Rowe, M. Wong, C. Cooper, D. Sergatskov, D. Bice, Y. Trenikhina *et al.*, arXiv:1305.2182.
- [56] J. W. Angle, E. M. Lechner, C. E. Reece, F. A. Stevie, and M. J. Kelley, *J. Vac. Sci. Technol. B* **41**, 034005 (2023).
- [57] W. Han and F. Fang, *Int. J. Mach. Tools Manuf.* **139**, 1 (2019).
- [58] S. Posen *et al.*, *Phys. Rev. Accel. Beams* **25**, 042001 (2022).
- [59] F. Furuta, D. Bice, A. Crawford, and T. Ring, in *Proceedings of International Conference on RF Superconductivity, SRF-2019, Dresden, Germany* (JACoW, Geneva, Switzerland, 2019), p. 453.
- [60] A. C. Crawford, *Nucl. Instrum. Methods Phys. Res., Sect. A* **849**, 5 (2017).
- [61] A. Prudnikava, Y. Tamashevich, S. Babenkov, A. Makarova, D. Smirnov, V. Aristov, O. Molodtsova, O. Kugeler, J. Viehhaus, and B. Foster, *Supercond. Sci. Technol.* **35**, 065019 (2022).
- [62] M. P. Do Carmo, *Differential Geometry of Curves and Surfaces: Revised and Updated Second Edition* (Courier Dover Publications, Garden City, NY, 2016).
- [63] J. E. Kuo, H. Wang, and S. Pickup, *Anal. Chem.* **63**, 630 (1991).
- [64] A. Savitzky and M. J. Golay, *Anal. Chem.* **36**, 1627 (1964).
- [65] B. W. Maxfield and W. L. McLean, *Phys. Rev.* **139**, A1515 (1965).
- [66] M. Martinello, A. Grassellino, M. Checchin, A. Romanenko, O. Melnychuk, D. A. Sergatskov, S. Posen, and J. F. Zasadzinski, *Appl. Phys. Lett.* **109**, 062601 (2016).
- [67] M. Tinkham, *Phys. Rev.* **110**, 26 (1958).
- [68] F. P.-J. Lin and A. Gurevich, *Phys. Rev. B* **85**, 054513 (2012).
- [69] J. Angle, M. Kelley, J. Tuggle, G. Eremeev, C. Reece, and U. Pudasaini, in *Proceedings of International Conference on RF Superconductivity, SRF-2019, Dresden, Germany* (JACoW, Geneva, Switzerland, 2019), p. 871.
- [70] J. W. Angle, A. D. Palczewski, C. E. Reece, F. A. Stevie, and M. J. Kelley, *J. Vac. Sci. Technol. B* **39**, 024004 (2021).
- [71] J. W. Angle, E. M. Lechner, A. D. Palczewski, C. E. Reece, F. A. Stevie, and M. J. Kelley, *J. Vac. Sci. Technol. B* **40**, 024003 (2022).
- [72] J. W. Angle, Trace level impurity quantitation and the reduction of calibration uncertainty for secondary ion mass spectrometry analysis of niobium superconducting radio frequency materials, Ph.D. thesis, Virginia Tech, 2022.
- [73] J. T. Maniscalco, S. Aderhold, T. T. Arkan, D. Bafia, M. E. Bevins, M. Checchin, A. Cravatta, D. Gonnella, A. Grabowski, J. Hogan, J. Kaluzny, R. D. Porter, S. Posen, C. E. Reece, and J. Venekate, in *Proceedings of the SRF'23* (JACoW Publishing, Geneva, Switzerland, 2023).
- [74] J. Maniscalco, S. Aderhold, T. Arkan, M. Checchin, J. Fuerst, D. Gonnella, J. Hogan, J. Kaluzny, A. Palczewski, S. Posen *et al.*, in *Proceedings of 20th International Conference on RF Superconductivity, SRF2021, East Lansing, MI* (JACoW, Geneva, Switzerland, 2022), 10.18429/JACoW-SRF2021-THPCA009.
- [75] B. Aune, R. Bandelmann, D. Bloess, B. Bonin, A. Bosotti, M. Champion, C. Crawford, G. Deppe, B. Dwersteg, D. A. Edwards *et al.*, *Phys. Rev. ST Accel. Beams* **3**, 092001 (2000).

- [76] T. Kubo, *Phys. Rev. Res.* **2**, 033203 (2020).
- [77] C. Reece, J. Angle, E. Lechner, A. Palczewski, F. Stevie, and M. Kelley, in *Proceedings of 13th International Particle Accelerator Conference, IPAC-2022, Bangkok, Thailand (JACoW, Geneva, Switzerland, 2022)*, [10.18429/JACoW-IPAC2022-TUPOTK042](#).
- [78] U. Pudasaini, G. V. Ereamev, J. W. Angle, J. Tuggle, C. E. Reece, and M. J. Kelley, *J. Vac. Sci. Technol. A* **37**, 051509 (2019).
- [79] C. Pira, C. Antoine, E. Chyhyrynets, X. Jiang, A. Katasevs, J. Kaupužs, O. Kugeler, S. Leith, O. Malyshev, A. Medvids *et al.*, in *Proceedings of 19th International Conference on RF Superconductivity, SRF'19, Dresden, Germany (JACoW, Geneva, Switzerland, 2019)*, p. 935.
- [80] A.-M. Valente-Feliciano, *Supercond. Sci. Technol.* **29**, 113002 (2016).
- [81] T. Kubo, *Supercond. Sci. Technol.* **30**, 023001 (2016).